Sustainable Structures
ISSN: 2789-3111 (Print); ISSN: 2789-312X (Online)
http://www.sustain-dpl.com/journal/sust
DOI: 10.54113/j.sust.2025.000085

ORIGINAL ARTICLE

Experimental and theoretical study of replaceable energy-dissipation devices for beam-column joints under cyclic loads

Hongchao Guo[a,b,*], Yuwei Li [b], Dongdong Zheng[b], Wenqi Wang[b], Renzhang Song[b], Yunhe Liu[a]

[a] State Key Laboratory of Water Engineering Ecology and Environment in Arid Area, Xi'an University of Technology, Xi'an 710048, PR China
[b] School of Civil Engineering and Architecture, Xi'an University of Technology, Xi'an 710048, PR China
[*]Corresponding Author: Dr. Prof. Hongchao Guo. Email: ghc-1209@163.com

Abstract: This paper presents two types of metal dampers for beam-column joints based on the replaceability design concept after an earthquake. A low-cyclic loading test of slit/corrugated dampers was conducted, revealing the failure and load-bearing mechanisms. The distribution of shear loads on steel hinges, slit plates, and corrugated plates at varying displacements was examined. A finite element (FE) model incorporating the Chaboche constitutive was established. The influence of geometrical parameters, including the T-stiffened plate, slit plate, and corrugated plate, on the peak bearing capacity and initial stiffness of metal dampers is discussed in detail. The results show that the peak bearing capacity of the damper is negatively correlated with the aspect ratio of the T-stiffening plate, which is recommended to be limited to 1.27. Increasing the thickness of the T-stiffened plate can effectively delay damage to the slit plate and corrugated plate. It is advised that the thickness of the T-stiffened plate should exceed that of the corresponding slit and corrugated plates. Increasing the thickness of corrugated plates from 3mm to 9mm delays buckling and increases initial stiffness by 15.34% and 10.91%, respectively. The skeleton curve model for the metal damper was established, providing both experimental and theoretical references for slit and corrugated metal dampers in engineering applications.

Keywords: Slit damper, corrugated damper, sustainable structures, initial stiffness, skeleton curve model

1 Introduction

The mechanical properties of the beam-column joint, a critical component in the frame's plastic deformation, significantly influence the structural system. In conventional frame structures, ductile design is commonly achieved by reinforcing the joint areas or weakening the beam flange, which allows for outward displacement of joint plastic hinges [1][3]. Nonetheless, substantial damage accumulates in the plastic hinge region during intense earthquakes, resulting in considerable residual drift and complicating repair efforts [4][5]. Consequently, numerous scholars have studied self-centering mechanisms [6][8], replaceable members [9][11], and rocking configurations [12] to mitigate residual drift and facilitate expedited restoration of structural functionality. These investigations aim to enhance the resilience and promote the sustainable development of building structures.

Received: 24 November 2024; Received in revised form: 4 April 2025; Accepted: 8 August 2025

The replaceability structural components, utilizing angle steel [13][14] and T-type steel [15][16], are designed to concentrate damage and dissipate seismic energy, significantly reducing the potential harm to structural and non-structural elements. The choice of metal-yielding dampers represented an optimal low-cost solution requiring little maintenance and easy replaceability in case of damage [17]. Wang et al. [18][19] introduced an external replaceable energy-dissipating device (EREDD). This device enhances the seismic performance of prefabricated segmental concrete-filled steel tubular bridge piers ((PS-CFST bridge piers) while focusing damage on easily replaceable components. By concentrating damage in these components, the EREDD achieves controlled damage, facilitating efficient post-earthquake repairs and maintenance. Hu et al. [20] developed a bending moment-shear separation controllable plastic hinge using replaceable multi-slit energy dissipation devices. This allows the precast joint to have excellent ductility and energy dissipation with damage concentrated on the multi-slit devices. Li et al. [21] proposed prefabricated beam-column steel joints with a damper, where the damper is selected from low-yield point steel to provide energy dissipation capacity. Compared to monolithic joints, these joints have the advantages of easy fabrication, high initial stiffness, and effective control of the position of the plastic hinge. Xie et al. [22] proposed a precast concrete frame (PCF) with replaceable energy-dissipation connectors (REDCs), where a steel hinge meets the shear-resistance demand of the beam end. The REDCs are used as moment-resisting and energy-dissipating members. Repairing the PCF after an earthquake only requires replacing the damaged REDC. Du et al. [23] proposed a replaceable graded-yielding energy-dissipating connector (RGEC) arranged at the beam end to dissipate energy and transfer the beam end loads through steel hinges. The results demonstrate that the graded yielding design of RGEC can be adapted to different seismic risks and achieve the desired seismic design. Yang et al. [24] proposed a double-stage-behavior dry-connected beam-column joint (DADBJ), which is connected by a rotational friction hinge (RFH) and a slitted buckling restrained steel plate (SBRSP). As displacement increases, the energy dissipation mechanism transitions from RFH alone to SBRSP and RFH together. Previous studies suggest that some researchers have refined the design of beam-column joint configurations by incorporating single or multiple yielding mechanisms. These modifications can promote improved energy dissipation and damage concentration within specified areas. However, the load-bearing and energy-dissipation capabilities of the joint region are contingent upon a solitary damaged component, which reduces the joint's safety redundancy in the context of intense seismic activity or post-earthquake effects. Additionally, steel hinges can better withstand shear demands at the beam end. When replacing the energy-dissipating devices at the top and bottom of the beam ends, additional equipment was required to limit the rotation of the steel hinges, complicating rapid structure repair.

Motivated by the deficiencies mentioned above, this paper studies a series of metal dampers suitable for post-earthquake recoverable beam-column joints, namely replaceable double-damage element energy dissipation devices with steel hinges, as shown in **Fig. 1**. The beam-column members are simplified, retaining only the joints in the energy-dissipating regions. The double-damage element, comprising two T-shaped stiffener plates and two slit/corrugated plates, is demonstrated to be highly effective in optimizing the joint's bearing capacity and energy-dissipation mechanism, thereby enhancing safety redundancy. The plastic resistance moment provided by the T-stiffened plate is converted by its axial force into a force couple. The slit plate/corrugated plate is subjected to bending-shear coupled loading. Integrating steel hinges into the energy-dissipating device facilitates the separation of bending and shear forces, effectively mitigating the degradation of peak bearing capacity associated with bending-shear coupling. A finite element (FE) model incorporating the Chaboche constitutive model has been established. The influence of geometrical parameters, including the T-stiffened plate, slit plate, and corrugated plate, on the peak bearing capacity and initial stiffness of metal dampers is discussed in detail. The initial stiffness model and the bearing capacity calculation formula for the damper have been derived. The skeleton curve model of the metal damper is established, providing both experimental and theoretical data for the engineering application of slit and corrugated metal dampers.

2. Experiment overview

2.1 Specimen design and loading scheme

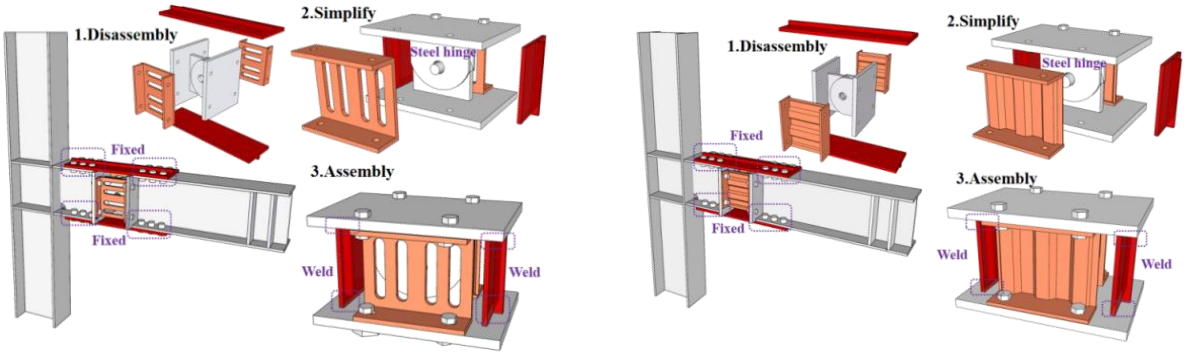

(a)Slit damper (b)Corrugated damper

Fig.1 Joint simplification damper

Fig. 2 illustrates the slit damper and corrugated damper. The metal damper consists of two regions: an energy dissipation area, composed of T-stiffened plates, slit plates, or corrugated plates, and a connection area, consisting of connecting plates, ear plates, hinges, and high-strength bolts of grade 10.9. Slit plates and corrugated plates are positioned within the beam web. These components are characterized by their ability to enhance energy dissipation capacity and out-of-plane stiffness. Under cyclic loading, the axial force of the T-shaped stiffener plate forms a force couple, resisting bending moment with the slit/corrugated plate. The steel hinge shares part of the shear force, placing the slit and corrugated plates in a bending-shear composite force state. **Fig. 2**(d) shows the dimensions of each component. The T-stiffened plate, slit plate, and corrugated plate are made of Q235 steel, with a thickness of 10mm, except for the 3mm thick corrugated plate. The connection area is made of Q355 steel. The yield strength f_y, and ultimate strength fu of Q235 steel were obtained from material property tests, where f_y and f_u of 3mm steel were 265MPa and 420MPa, respectively; f_y and f_u of 10mm steel were 300MPa and 465MPa, respectively.

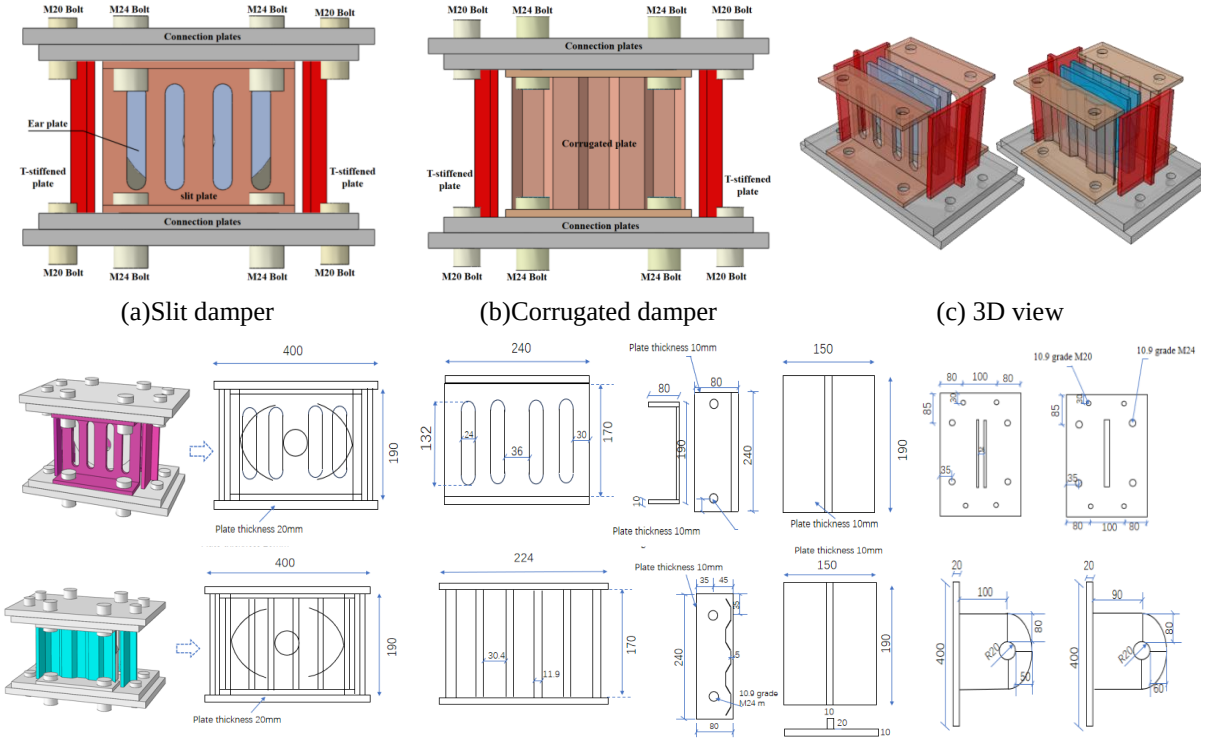

(a)Slit damper (b)Corrugated damper (c) 3D view

(d) Specimen size (Unit: mm)

Fig.2 Details of tested specimens

A beam-column inversion method was employed in the joint testing, where loading was applied at the beam ends. The metallic damper testing simplified non-energy-dissipating components such as beams and columns. An equivalent-length steel beam, similar to that used in the joint tests, was utilized

as the loading apparatus. This approach was adopted to investigate the seismic performance of metallic dampers. The lower connecting plate of the metal damper was affixed to the base beam, and an upper loading beam was attached to the damper to interface with the MTS actuator. The loading protocol employed a quasi-static cyclic method under displacement control [25], with the test setup and loading procedure illustrated in **Fig. 3**. The loading was terminated either upon specimen fracture or when the load decreased to 85% of its peak bearing capacity. Strain measurements in the steel were obtained using two distinct systems: the Donghua 3816 Dynamic Data Acquisition Instrument and the VIC-3D non-contact measurement system.

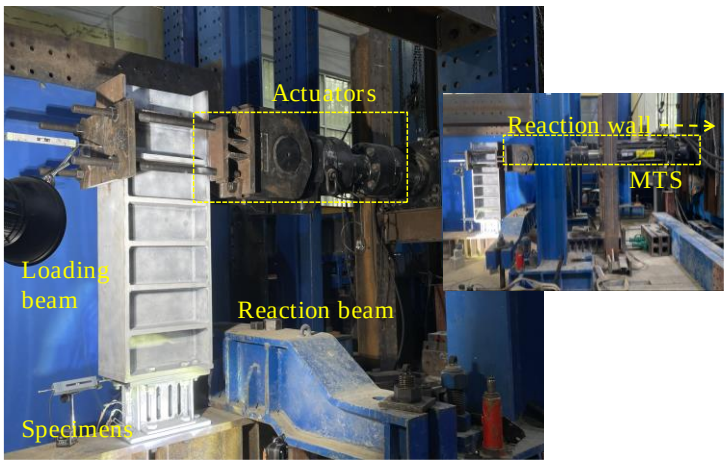

Fig.3 Details of loading setup

2.2 Test results

The two metal dampers exhibit distinct yielding behavior under external loads. Incorporating strain data and experimental observations, it is noted that the T-stiffening plate and the slit plate yield varying displacement levels. Energy dissipation is facilitated by the synergistic interaction of these two components. Despite corrugated plates having high out-of-plane stiffness, their thin 3mm thickness results in an indistinct yielding sequence between the T-stiffened and corrugated plates. **Fig. 4** illustrates the failure mode of the metal damper. The T-stiffened plate of both damper categories undergoes obvious bending deformation, and the T-stiffened plate of the slit damper and the upper and lower connecting plates are connected to the position of weld cracking. Prominent out-of-plane buckling distortion was observed in the ribs of the slit plate, whereas the central ribs remained largely unaffected. The corrugated plate exhibits out-of-plane buckling deformation only at the corners. Due to the steel hinges, neither the slit nor the corrugated plates showed noticeable plastic deformation in their central regions.

(a)Slit damper (b)Corrugated damper

Fig.4 Damage phenomenon

Fig. 5 illustrates the load-displacement curves of the test dampers. In particular, the hysteresis curves of the slit damper exhibit a more complete profile than those of the corrugated damper, indicating superior energy dissipation and enhanced load capacity. The yield point (Δ_y, P_y) of the skeleton curve is calculated using the generalized yield moment (GYM) method [26] within **Fig. 6**. The procedure of the GYM method for determining yield point (Δ_y, P_y) is as follows: (i) extend the tangent line (OA) to

intersect the horizontal line passing peak point (Δ_m, P_m) at point A; (ii) make the normal line through point A intersect at point B of skeleton curve; (iii) extend line OB to determine point C; (iv) the normal line passing point C intersects the skeleton curve at certain point that is the yield point (Δ_y, P_y). The results are presented in **Table 1**. The positive and negative peak bearing capacity P_m of the slit damper is observed to be 11.82% and 34.14% greater than that of the corrugated damper, respectively. In contrast, the ductility coefficients μ of the two categories of dampers are found to be relatively similar, with values of 5.48 and 5.28, respectively.

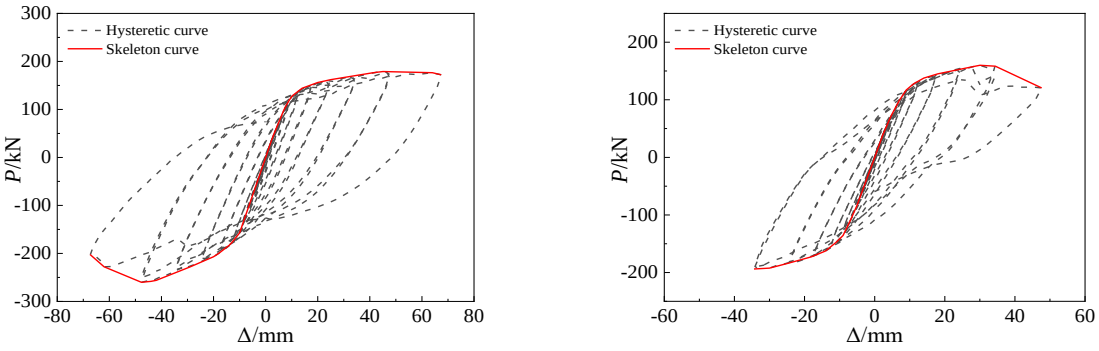

(a) Slit damper (b) Corrugated damper

Fig.5 Test curves

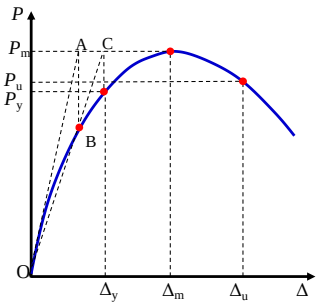

Fig.6 The generalized yield moment method

Table 1. Mechanical parameter

Specimen	Direction	K/kN·mm^{-1}	Δ_y/mm	P_y/kN	Δ_m/mm	P_m/kN	μ
Slit damper	+	19.087	10.20	152.90	45.02	178.80	5.48
	-		-12.32	-184.70	47.70	-260.10	
Corrugated damper	+	17.275	8.01	124.50	30.02	159.90	5.28
	-		-10.13	-157.40	-34.42	-193.90	

Note: K is the initial stiffness; P_y and P_m are the yield bearing capacity and peak bearing capacity of the energy-consuming device, respectively. Δ_y and Δ_m are the corresponding displacements of the energy-consuming device's yield and peak bearing capacity, respectively. μ is the ductility coefficient, $\mu=\Delta_u/\Delta_y$.

2.3 Force analysis of slit plates, corrugated plates, and steel hinges

The force analysis is depicted in **Fig. 7**, where the plastic resistance moment provided by the T-stiffened plate is converted by its axial force into a force couple. The slit plate and corrugated plate are subjected to bending-shear coupling. It is assumed that the T-stiffened plate is subjected to axial forces only, so the beam end shear forces are carried by the steel hinges and the slit/corrugated plate, resulting in both the slit plate and the corrugated plate being in composite stresses. The shear capacity percentages of the steel hinges and slit/corrugated plates are determined. Using the stress-strain equations of steel from the literature [27], combined with P-Δ curves and strain data of the T-stiffened plate, the force trends of the steel hinges and plates under different displacements are calculated as (1)-(6).

$$\sigma(\varepsilon)=\begin{cases}E_s\varepsilon\left(0\le\varepsilon\le\varepsilon_y\right)\\330.96+2213.46\varepsilon-6788.84\varepsilon^2-14203.91\varepsilon^3\left(\varepsilon_y\le\varepsilon\le\varepsilon_u\right)\end{cases} \tag{1}$$

$$M_{\text{flange}}=\sigma(\varepsilon)\cdot A_{\text{flange}}\cdot h_{\text{beam}} \tag{2}$$

$$M_{\text{load}} = F \cdot l \tag{3}$$

$$M_d = M_{\text{load}} - M_{\text{flange}} \tag{4}$$

$$F_{\text{s,d}} = M_d / l \tag{5}$$

$$F_{\text{s,hp}} = F - F_{\text{s,d}} \tag{6}$$

Where M_{load}, M_{flange}, and M_{d} are the bending moments of the damper, T-stiffened plate, and slit/corrugated plate, respectively; E_{s} is the modulus of elasticity; A_{flange} is the cross-sectional area of the T-shaped stiffener; F, $F_{\text{s,d}}$, and $F_{\text{s, hp}}$ are damper beam end loads, slit plate/corrugated plate loads and steel hinge loads, respectively; h_{beam} is the distance between two T-stiffened plates; l is the length of the beam.

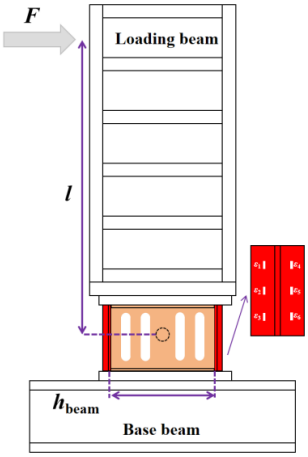

Fig.7 Load analysis diagram of metal damper

Fig. 8 presents the calculation results. At the start of loading, the slit plate and corrugated plate experienced shear loads of 18% and 33%, respectively, reflecting the graded yielding behavior of the slit damper. As displacement increased, the percentage of shear force borne by the slit/corrugated plate gradually rose. As the displacement increases, the proportion of shear force borne by the slit plates gradually rises. In contrast, the percentage of shear force carried by the corrugated plates remains relatively limited. Analyzing this behavior reveals that the ribs of the slit plate gradually expanded from the edge to the middle position, causing the shear force percentage to increase and decrease after failure. As a primarily shear-bearing component, the steel hinge had a shear force share of 55% to 87%.

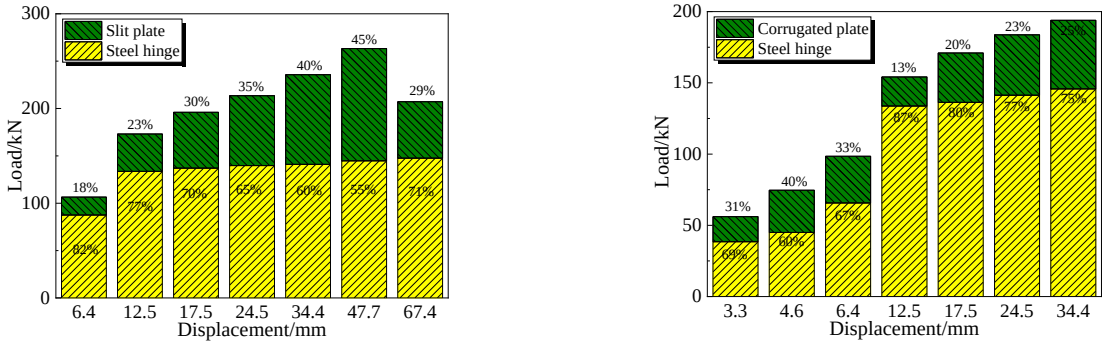

(a)Slit damper (b)Corrugated damper

Fig.8 Steel hinge bearing capacity contribution

3. Numerical simulation on cyclic behavior

A finite element (FE) model was established to evaluate metal dampers' nonlinear and cyclic hardening behavior subjected to combined bending load. This model comprehensively analyzes the influence of geometric parameters of T-stiffened plates, slit plates, and corrugated plates, thereby serving as a critical reference for advancing theoretical computations.

3.1 FE model building

Within the material constitutive model, the Chaboche constitutive model is utilized for steels in energy dissipation areas [28], including T-stiffened plates, slit plates, and corrugated plates. For the connection areas, a bilinear kinematic hardening model is selected for the steel and the bolts. Detailed parameter settings are provided in **Table 2** and illustrated in **Fig. 9**. The model's boundary conditions are set according to the experimental setup shown in **Fig. 3**. To enhance computational efficiency and minimize time expenditure, the FE model focuses on a refined representation of the metal damper. It sets the coupling constraint point in the upper part of the damper rather than modeling the load transfer through the loading beam. The simulation and analysis follow the test loading rules, with the bottom of the damper constrained in all degrees of freedom, rather than modeling the base beam.

Table 2. Parameter of Chaboche model[29]

Material	$\sigma\|_0$	Q_∞	b_{iso}	$C_{kin,1}$	γ_1	$C_{kin,2}$	γ_2	$C_{kin,3}$	γ_3	$C_{kin,4}$	γ_4
Q235-3	265	21	1.2	6013	173	5024	120	3026	32	990	35
Q235-10	300	21	1.2	7993	175	6773	116	2854	34	1450	29

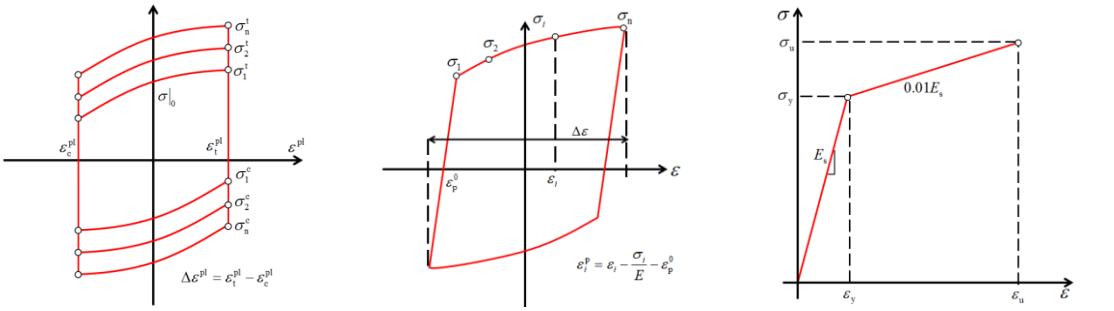

(a)Chaboche model (b) A bilinear kinematic hardening model

Fig.9 Constitutive relation curve

The contact surfaces between the slit plate and the junction plate and between the bolt and the steel plate are defined as general contacts. Hard contact is selected for normal behavior, while for tangential behavior, the penalty function method is used with a friction coefficient of 0.3 [30]. The corrugated plate and end flange are connected by a "Tie" constraint representing a welded joint. A hinge connection type is selected for the pin at the center of the ear plate. To ensure the convergence and accuracy of the computations, hexahedral meshes and structured meshing techniques were employed in the mesh generation process. As shown in **Fig. 10**, each component is modeled and analyzed using C3D8R solid elements. Mesh convergence analysis determined a suitable mesh density of 5 mm. The hysteresis performance of the metal damper under bending cyclic load was then tested using a generic static simulation.

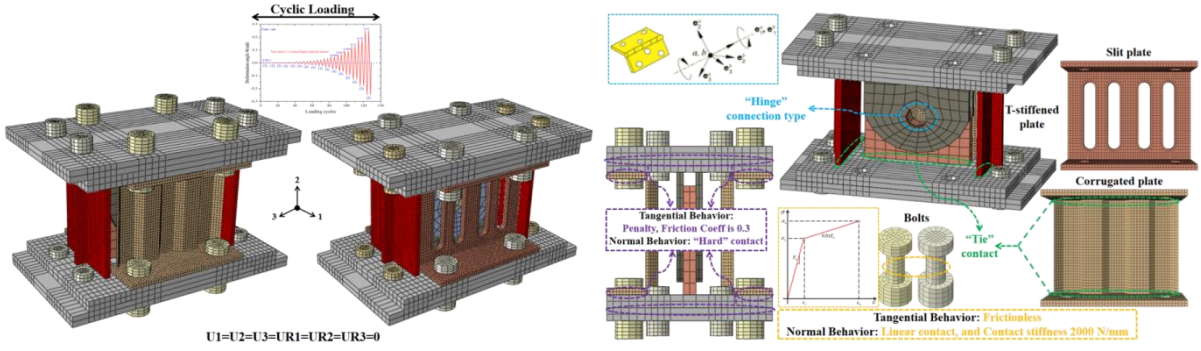

(a)Boundary conditions (b)Interactions

Fig.10 FE model of damper

3.2 Verification of FE model

The FE model results were compared with experimental results. The metal dampers ' typical failure modes and *P*-Δ curves are compared in **Figs. 11** and **12**. The simulated hysteresis curve is essentially in agreement with the experimental curve, and the established FE model can accurately simulate the mechanical characteristics of such dampers under cycle load. In **Table 3**, the negative skeleton curve of the test is selected to compare with the simulated value. Except for the peak bearing capacity of the slit damper, which showed a relatively large error, the other points matched well. Due to uncontrollable factors such as test errors, the difference between the positive and negative bearing capacities of the hysteresis curve of the metal damper is significant. In contrast, the FE model, being more idealized, leads to certain inaccuracies between the simulated and experimental results. Nonetheless, since simulations do not account for initial defects and the cumulative development of damage in the steel, discrepancies remain between the simulated post-peak hysteresis behavior and test observations.

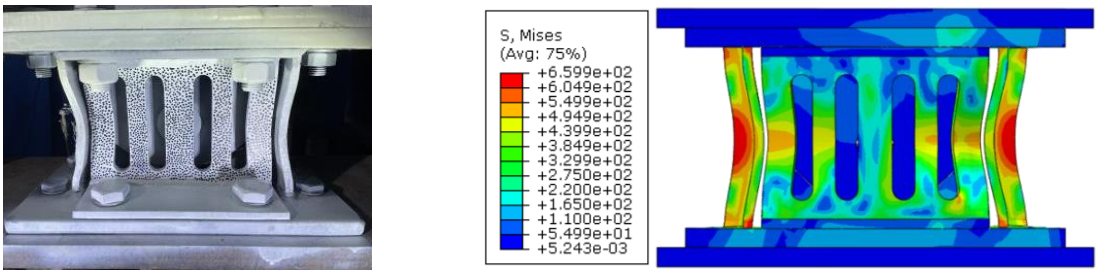

(a)Slit damper

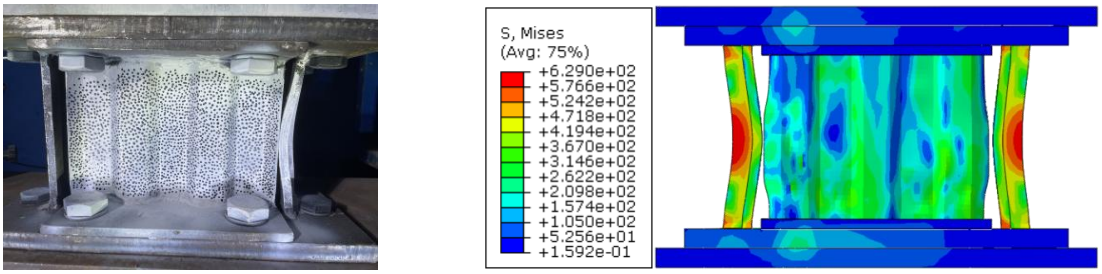

(b)Corrugated damper

Fig.11 Comparison of failure mode

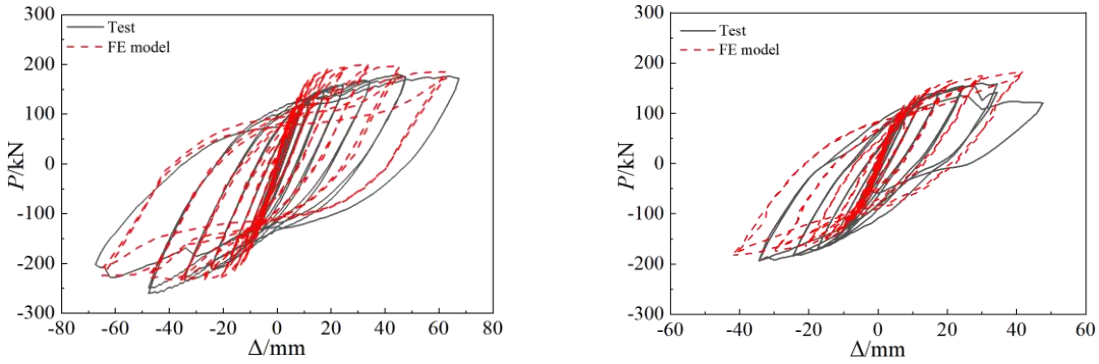

(a)Slit damper

(b)Corrugated damper

Fig.12 Comparison of hysteretic curves

Table 3. Comparison between test and FE model

	Slit damper		Corrugated damper	
	P_y/kN	P_m/kN	P_y/kN	P_m/kN
Test	184.70	260.10	157.40	193.90
FE model	179.01	226.64	144.64	182.56
Test /FE model	1.03	1.15	1.09	1.06

3.3Damage behavior analysis

To analyze the yielding and plastic behavior of metal dampers under cyclic load, we discuss slit and corrugated dampers separately.

3.3.1 Slit damper

Fig. 13 shows the loading process of the slit damper FE model, which is divided into several stages. After applying preload to the high-strength bolts, bending cyclic loading begins. At displacements below 2.3 mm, the slit dampers are in an elastic state. At a displacement of 4.6 mm, the corners of the T-stiffened plate and the stiffening ribs reach their yield point. With increasing displacement, the yield zone widens. At a displacement of 6.4 mm, the rib yields under tension and compression, combined with the slit plate stress program. At a displacement of 9 mm, the yield area of the T-stiffened plate expands continuously from the corner to the center, with a larger yield area in the lower part than in the upper part. By this stage, the stiffening ribs of the T-stiffened plate have undergone complete cross-sectional yielding. Observing the plastic deformation of the slit damper, it can be seen that when the displacement reaches 12.5 mm, the T-stiffened plate is in full-section yielding. At this stage, the second rib of the slit plate likewise yields, and the plastic strain accumulates continuously. When the displacement is 24.5 mm, the plastic strain at the weld of the T-stiffened plate increases, and the plastic strain distribution of the ribs at the edge of the slit plate has been extended to the center of the plate, leading to buckling deformation. When the displacement is 47.7 mm, the plastic strain of the rib at the edge of the slit plate reaches 0.206-0.225, indicating failure according to the material property experiment. At a displacement of 67.4 mm when the loading ends, the slit plate, except for the rib at the center of rotation, exhibits apparent plastic accumulation and failure. Stress concentration at the weld of the T-stiffened plate leads to severe plastic deformation, and this failure mode in the FE model is consistent with the weld fracture observed in the experiment. The slit damper exhibits significant stepwise yielding and failure under cyclic loading, with both the T-stiffened plate and the slit plate undergoing yielding deformation under vertical tension and compression.

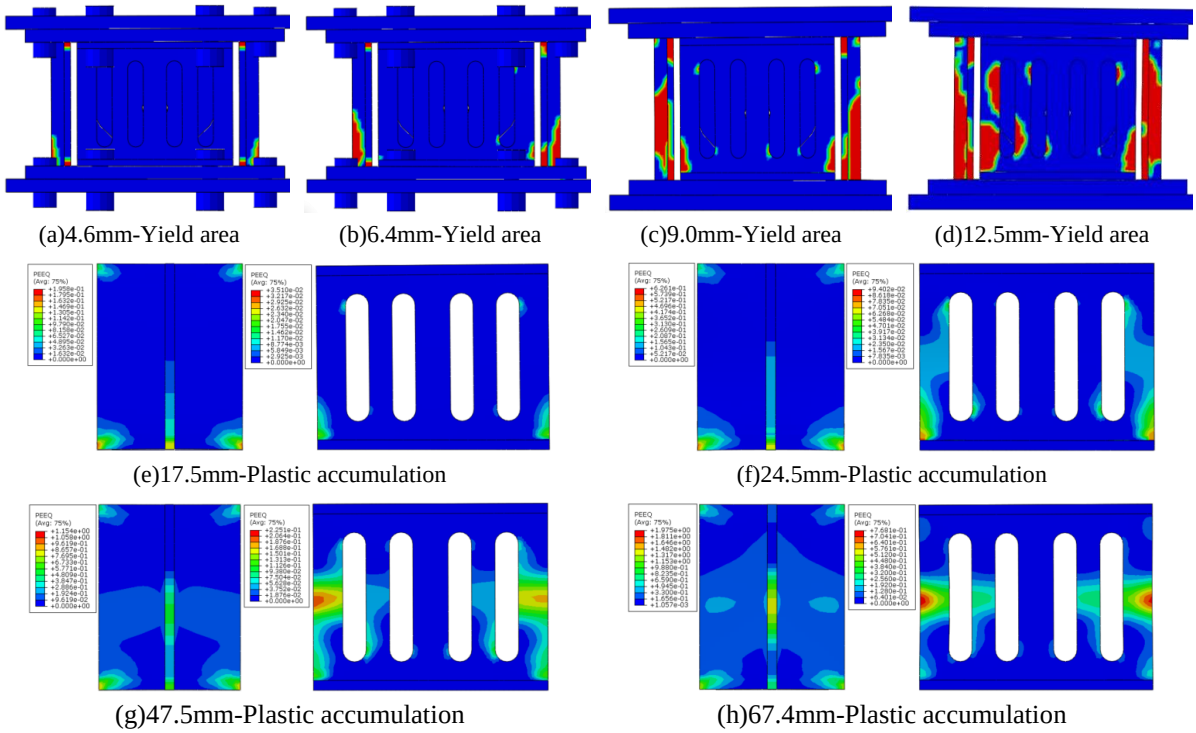

(a)4.6mm-Yield area (b)6.4mm-Yield area (c)9.0mm-Yield area (d)12.5mm-Yield area

(e)17.5mm-Plastic accumulation (f)24.5mm-Plastic accumulation

(g)47.5mm-Plastic accumulation (h)67.4mm-Plastic accumulation

Fig.13 Slit damper

3.3.2Corrugated damper

Fig. 14 shows that the corrugated damper behaves differently from the slit damper under bending cyclic load. At a displacement of 3.3 mm, the T-stiffened plate and the corners of the corrugated plate

reach their yield stresses simultaneously and expand toward the center, respectively. At 9 mm displacement, the yielding of the T-stiffened plate forms an "X" shape, and the right side of the corrugated plate yields extensively. Observing the plastic deformation of the corrugated damper, it can be seen that at 17.5 mm displacement, the corrugated plate wave peaks and valleys adjacent to the beveled edge exhibit plastic deformation ranging from 0.0901 to 0.0983, and simultaneously, the edge of the corrugated plate shows localized buckling. At 24.5 mm displacement, the T-stiffened plate exhibits apparent bending, and the plastic strain in the corner and middle of the stiffening rib exceeds 0.2, indicating a gradual decrease in the stiffness of the T-stiffened plate. At the same time, the corrugated plate exhibits obvious buckling deformation in the corner. At 34.4 mm displacement, severe plastic damage occurs at the edges and valleys of the corrugated plate, with plastic strains ranging from 0.245 to 0.267. The loading ends at 47.7 mm displacement. The T-stiffened plate and the corrugated plate yield almost simultaneously under bending load, and no obvious plastic deformation is observed in the center of the corrugated plate due to the presence of hinges.

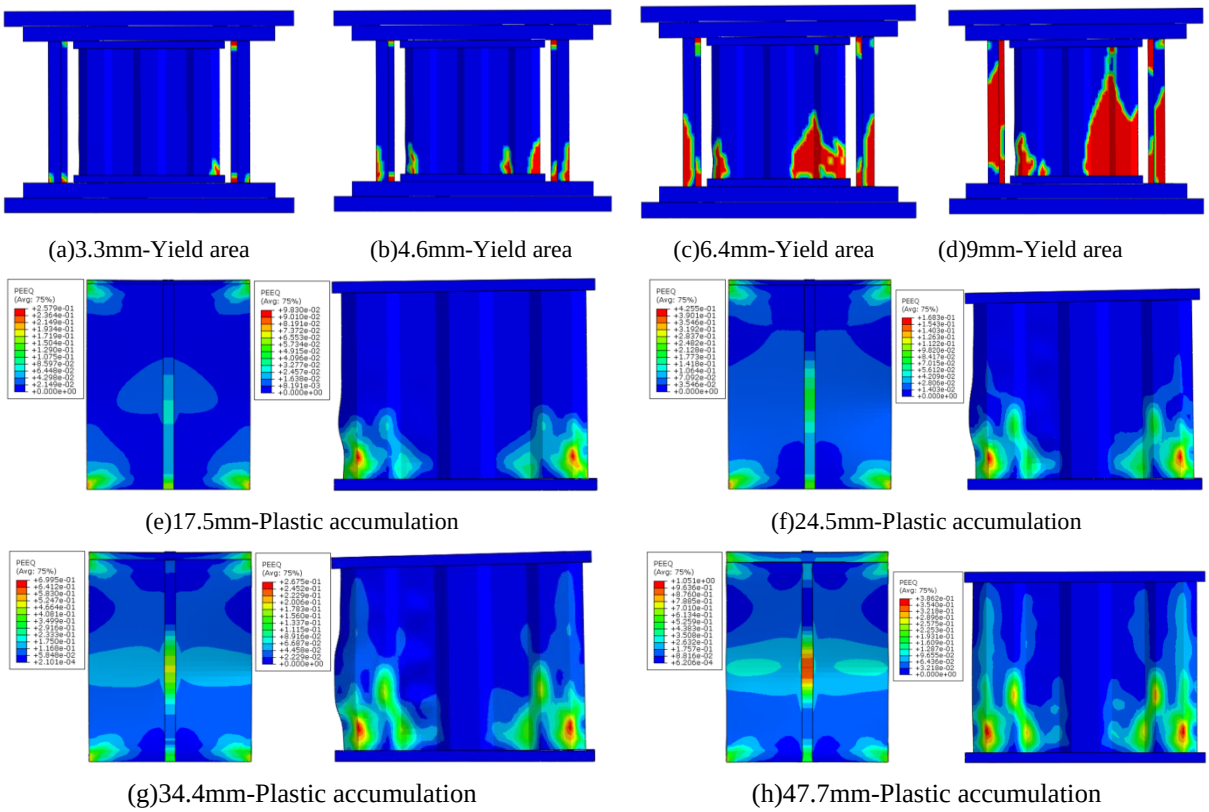

(a)3.3mm-Yield area (b)4.6mm-Yield area (c)6.4mm-Yield area (d)9mm-Yield area

(e)17.5mm-Plastic accumulation (f)24.5mm-Plastic accumulation

(g)34.4mm-Plastic accumulation (h)47.7mm-Plastic accumulation

Fig.14 Corrugated damper

3.4 Parametric study

The performance of the metal damper is primarily determined by the geometrical parameters of the T-stiffened plate, the slit plate, and the corrugated plate, as verified by the FE model. Therefore, the parametric analysis in this section primarily investigates the aspect ratio and thickness of the T-stiffened plate, the thickness of the slit plate and the corrugated plate, and the perforation rate, as detailed in **Table 4**. The influence of these metal dampers on the key parameters is discussed as follows.

Table 4. Parameter Settings

Parameter	Basic specimen	parameter setting
Aspect ratio	1.27	0.83/1/1.9
T-stiffened plates thickness	10mm	8/12/14/16 mm
Slit /Corrugated thickness	10mm	(Slit damper)6/8/12/14 mm(Corrugated damper)6/9 mm
Perforation rate	10.8%	3.4% /8.3% 14.9% /23%

3.4.1Aspect ratio of T-stiffened plate

As shown in **Fig. 15**, increasing the aspect ratio of the T-stiffened plate from 0.83 to 1.9 results in a gradual expansion of stress distribution from the sides of the stiffener to the entire section. Notably, the peak bearing capacity of the T-stiffened plate significantly decreases with increasing aspect ratio. For example, raising the aspect ratio from 1.27 to 1.9 reduces the peak carrying capacity P_m of slit and corrugated dampers by 15.86% and 16.76%, respectively. The aspect ratio has a minor effect on initial stiffness, which varies by no more than 7%. Therefore, increasing the aspect ratio of the T-stiffened plate decreases the peak bearing capacity and energy-dissipation capacity of the metal damper, leading to premature concentration of plastic damage in the slit plate and corrugated plate. To ensure better peak bearing capacity and energy dissipation of the metal damper, it is recommended that the aspect ratio of the T-stiffened plate does not exceed 1.27.

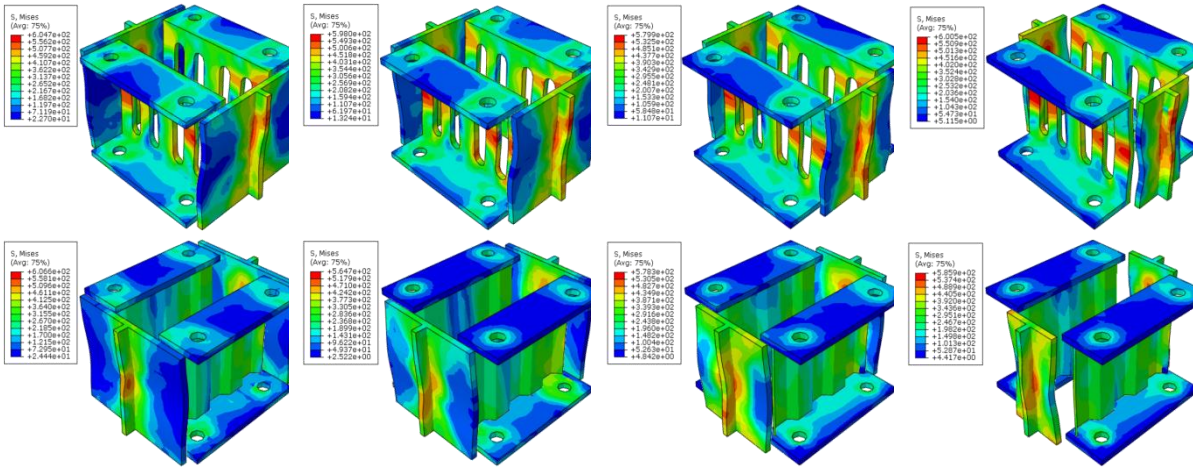

(a)Aspect ratio0.83 (b)Aspect ratio1.0 (c)Aspect ratio1.27 (d)Aspect ratio1.9

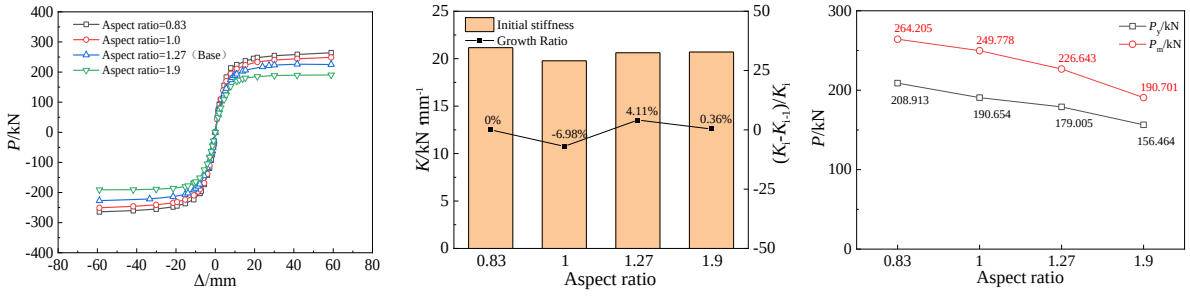

(e)Slit damper

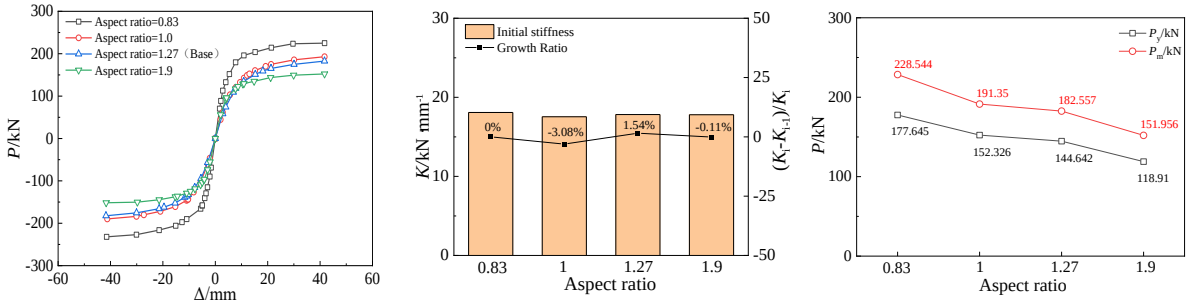

(f)Corrugated damper

Fig.15 Influence of aspect ratio

3.4.2Thickness of T-stiffened plate

Although the aspect ratio of the T-stiffened plate is constant, the influence of the T-stiffened plate thickness on the hysteresis performance of the metal damper is illustrated in **Fig. 16**. Slit plate plasticity develops more rapidly when the T-stiffened plate thickness is less than the slit plate thickness, a phenomenon similar to the increase in the T-stiffened plate aspect ratio. As the thickness of the T-stiffened plate increases from 8 mm to 16 mm, the initial stiffness improves gradually; for example, the

growth rate of the initial stiffness of the slit damper is 4.9%, 8.47%, 4.02%, and 3.49%, respectively. The peak bearing capacity increases substantially with increasing thickness, and the rate of increase tends to stabilize. Combined with the plastic strain distribution diagrams, the increased thickness of the T-stiffened plate delays slit and corrugated plate damage while significantly raising the overall energy dissipation capacity of the metal damper. Therefore, it is recommended that the thickness of the metal damper T-stiffened plate not be less than the thickness of the slit plate and corrugated plates. It is advisable that the thickness of the T-stiffened plate in metal dampers not be less than that of the slit or corrugated plates. To maximize the energy dissipation potential of the steel, it is advisable not to exceed a thickness of 16 mm.

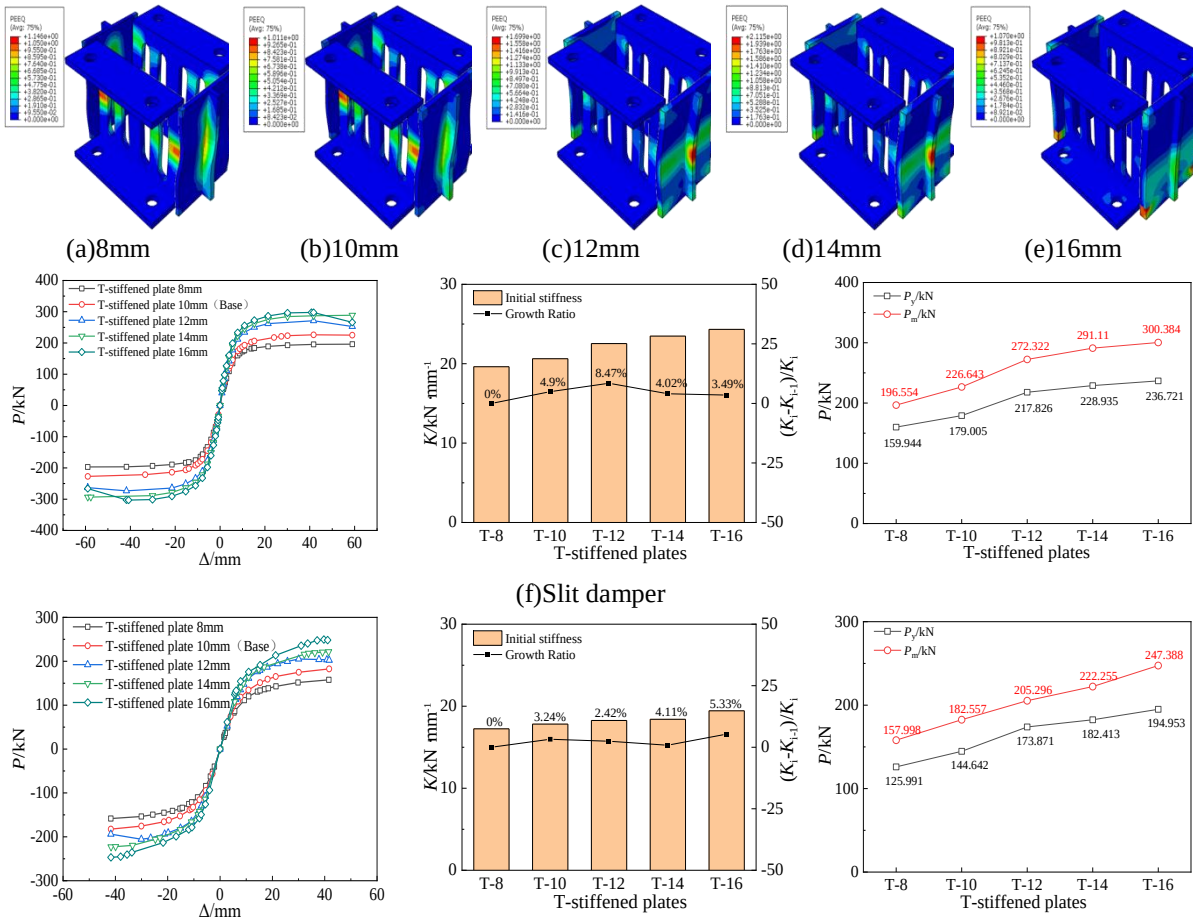

Fig.16 Influence of T-stiffened plate thickness

3.4.3 Thickness of slit/corrugated plate

Fig. 17 illustrates the influence of slit and corrugated plate thickness on the mechanical properties of the metal damper. While increasing the thickness of the slit and corrugated plates does enhance the peak bearing capacity of the metal damper, the improvement is less substantial than that observed with increasing T-stiffened plate thickness. With a slit plate thickness of 6 mm, the ribs are particularly susceptible to premature buckling, leading to premature failure of the metal damper system. Enhancing the slit plate thickness of the metal damper from 6mm to 14mm results in respective increments of 6.33%, 8.04%, 7.05%, and 6.25% in peak bearing capacity. At the same time, it effectively improves the energy absorption capacity of the slit plate and delays the buckling of the slit plate ribs. Regarding corrugated dampers, the corrugated plates, characterized by high out-of-plane stiffness, notably enhance initial stiffness. An increment in corrugated plate thickness from 3mm to 9mm resulted in respective increases of 15.34% and 10.91% in initial stiffness. Combined with plastic strain, the increase in the thickness of the corrugated plate can effectively alleviate corner buckling, so it is recommended that the thickness of the corrugated plate be higher than 3mm.

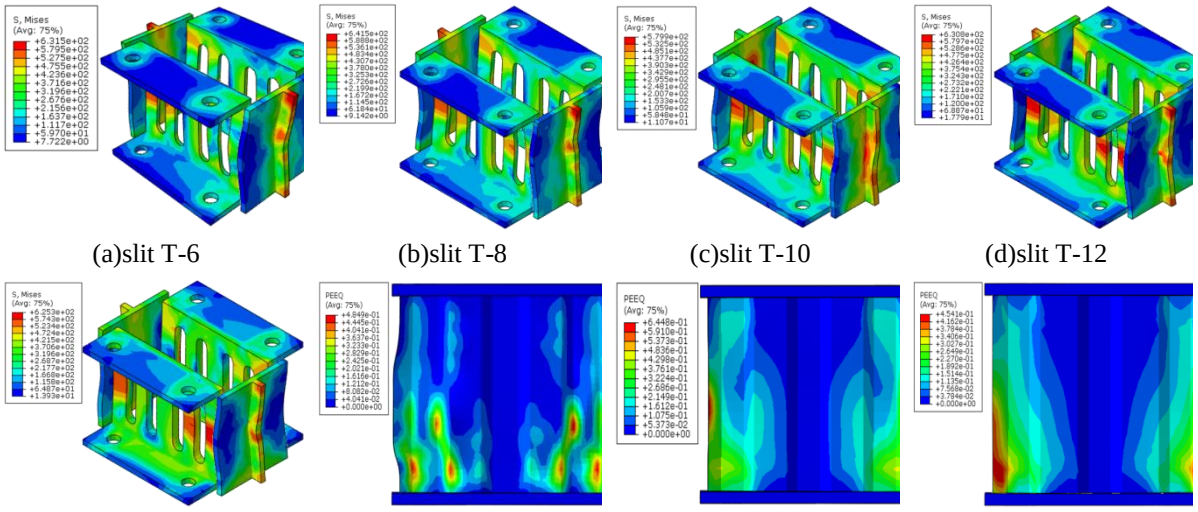

(a)slit T-6 (b)slit T-8 (c)slit T-10 (d)slit T-12

(e)slit T-14 (f)corrugated T-3 (g)corrugated T-6 (h)corrugated T-9

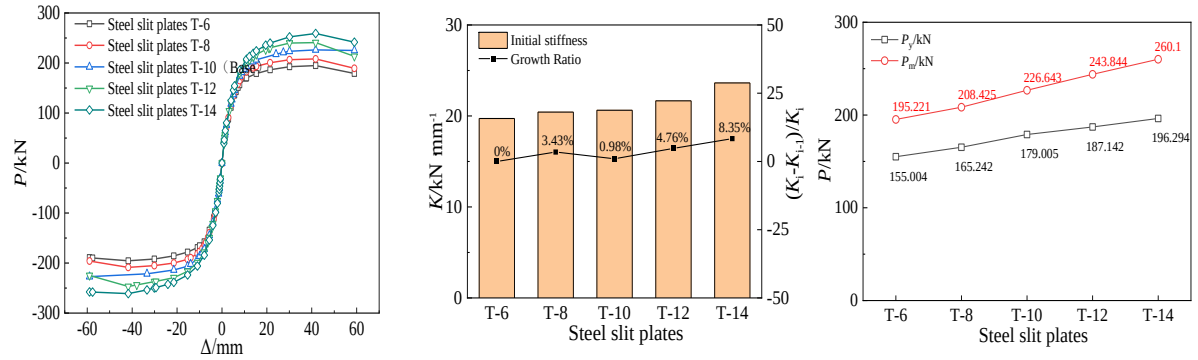

(i)Slit damper

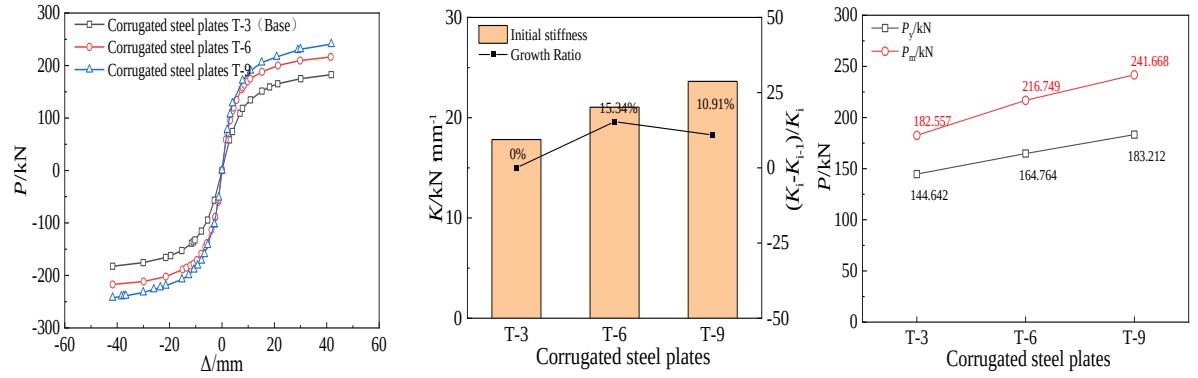

(j)Corrugated damper

Fig.17 Influence of shear plate thickness

3.4.4 Perforation rate

Fig. 18 illustrates the influence of the perforation ratio on the seismic performance of slit dampers. An increase in the perforation ratio significantly reduces the initial stiffness. E.g., increasing the perforation ratio from 8.3% to 10.8% results in a 9.2% reduction in initial stiffness. Similarly, an increase from 14.9% to 23% leads to a 14.85% decrease in initial stiffness. As the perforation ratio increases, the peak bearing capacity of the slit damper generally decreases, but the reduction is less pronounced compared to the initial stiffness. Specifically, increasing the perforation ratio from 8.3% to 10.8% results in a 1.64% reduction in peak carrying capacity. When the perforation ratio rises from 14.9% to 23%, the peak carrying capacity decreases by 6.57%. To optimize both the peak carrying

capacity and the deformation capability of slit dampers, it is recommended to limit the perforation ratio to a maximum of 14.9%.

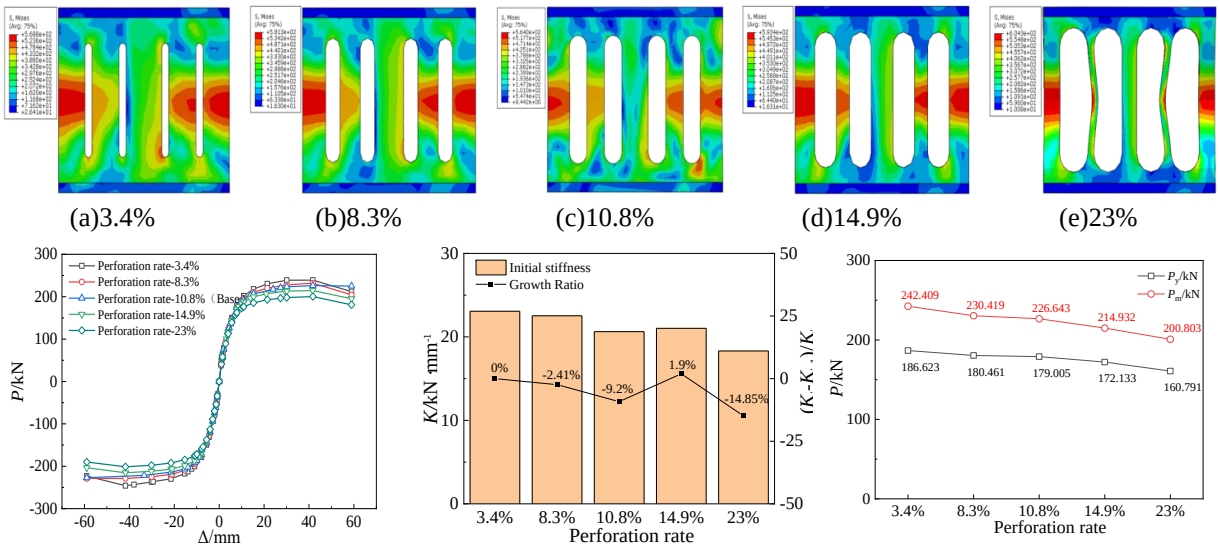

Fig.18 Influence of perforation rate

4. Initial stiffness, bearing capacity, and skeleton curve model

4.1Initial stiffness calculation model

Adopting the initial stiffness calculation model outlined in EC3 [31], the initial stiffness K_c of both slit and corrugated metal dampers is determined by Eq. (7). The metal damper components are arranged in series, with each element in parallel. Thus, the stiffness of each element is calculated and inputted into Eq. (7). The calculated stiffness values for individual components are depicted in **Fig. 19**.

$$K_c = \frac{L_p^2}{\mu \sum_i \frac{1}{K_i}} \tag{7}$$

Where L_p is the lever arm; μ is the stiffness ratio, take 1.0; K_i is the stiffness for basic component i.

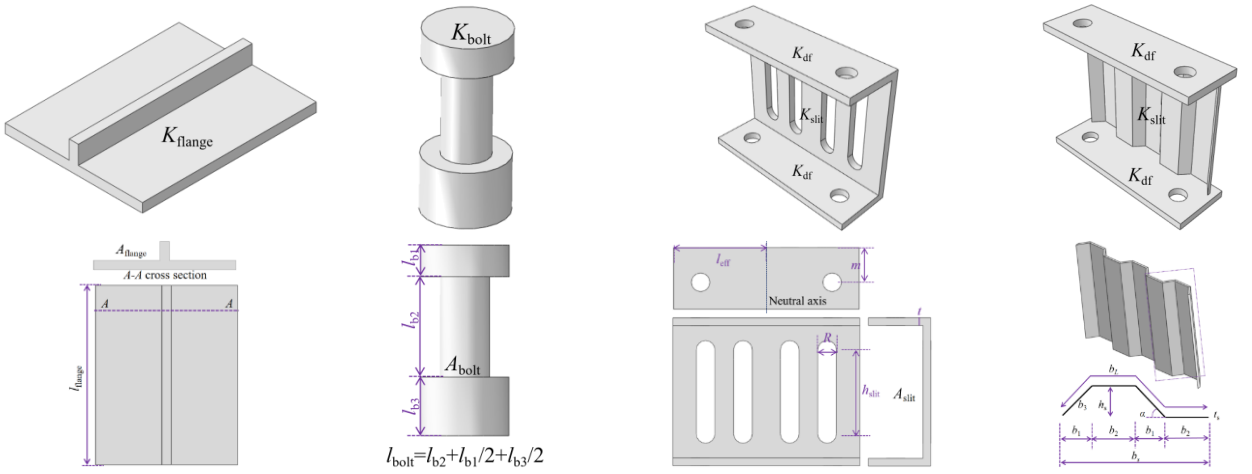

(a) T-stiffened plate (b) High-strength bolt (c) Slit plate (d) Corrugated plate

Fig.19 Basic component stiffness calculation

Eq. (8) shows the calculation formula for the initial stiffness K_{flange} of the T-stiffened plate.

$$K_{\text{flange}} = \frac{nEA_{\text{flange}}}{l_{\text{flange}}} \tag{8}$$

Where n is the number of T-stiffened plates; E is the elastic modulus of the steel plate; A_{flange} is the cross-sectional area of the T-stiffened plate; l_{flange} is the height of the T-stiffened plate.

The calculation formula for high-strength bolt stiffness K_{bolt} is shown in Eq. (9).

$$K_{\text{bolt}} = \frac{1.6EA_{\text{bolt}}}{l_{\text{bolt}}} \tag{9}$$

Where A_{bolt} is the tensile stress area of the bolt; l_{bolt}——is the bolt elongation length, taken as equal to the grip length (total thickness of material and washers), plus half the sum of the height of the bolt head and the height of the nut.

The K_{df} calculation formula for the stiffness of the connecting plate with slit and corrugated is shown in Eq. (10).

$$K_{\text{df}} = \frac{0.9El_{\text{eff}}t^3}{m^3} \tag{10}$$

Where l_{eff} is the effective length of the flange cleat; t is the thickness of the connecting plate clamp plate; m is the distance from the center of the bolt hole to the edge of the connecting plate.

The calculation formula for the slit plate stiffness is given by Eqs. (11)~(13) by K_{slit}.

$$K_{\text{slit}} = \frac{1}{\frac{l_{\text{slit}}}{nEA_{\text{slit}}} + \frac{l_{\text{slit}}}{nGA_{\text{slit}}}} \tag{11}$$

$$l_{\text{slit}} = h_{\text{slit}} + \frac{2R^2}{h_{\text{slit}} + 2R} \tag{12}$$

$$G = \frac{E}{2(1+\mu)} \tag{13}$$

Where A_{slit} is the cross-sectional area of the slit plate. l_{slit} is the effective height of the slit plate. h_{slit} is the length of the slit; R is the slit diameter; G is the shear modulus; μ is Poisson's ratio.

The corrugated plate stiffness $K_{\text{corrugated}}$ is calculated using Eqs. (14)-(17).

$$K_{\text{corrugated}} = \frac{1}{\frac{l_{\text{corrugated}}}{nEA_1} + \frac{l_{\text{corrugated}}}{nGA_2}} \tag{14}$$

$$A_1 = \frac{b_L}{b_s} \cdot 2 \cdot n \cdot (b_1 + b_2) \cdot t_s \tag{15}$$

$$b_L = 2n(b_2 + b_3) \tag{16}$$

$$A_2 = 2n(b_1 + b_2) \cdot t_s \tag{17}$$

Where $l_{\text{corrugated}}$ is the height of the corrugated plate; A_1 and A_2 are the corrugated plate's bending and shear cross-sectional areas, respectively.

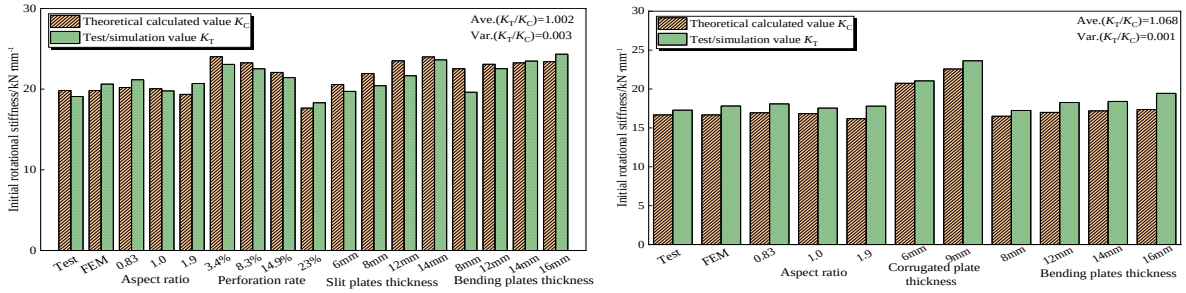

(a)Slit damper (b)Corrugated damper

Fig.20 Method verification by test and simulation

To validate the accuracy of the proposed method for calculating the initial stiffness of metal dampers, the theoretically calculated values for each component are compared with the experimental and numerical simulation values. The comparison results, shown in **Fig. 20**, indicate that the mean value and variance for the slit damper are 1.002 and 0.003, respectively, while for the corrugated damper they are 1.068 and 0.001. This demonstrates that the initial stiffness calculation formula presented in this paper can accurately evaluate the initial stiffness of both the slit and corrugated dampers.

4.2Metal damper bearing capacity calculation

In conjunction with Sections 2.2 and 3.3, it can be seen that the bearing capacity and energy dissipation of the metal damper at the point of yield is provided by the T-stiffened plate and the slit or corrugated plate. Under bending load, the T-stiffened and slit plates will have two modes of yielding, either strength yielding or plate buckling. In contrast, the corrugated plate has a high out-of-plane stiffness, so only its strength yielding is considered for the corrugated damper yielding capacity. As shown in **Fig. 21**, when the strength of the T-stiffened plate yields, the yield load is calculated as Eqs. (18) to (21), where A_{flange}, I_{flange}, and $I_{\text{b,flange}}$ are respectively the cross-sectional area of the T-stiffened plate, the moment of inertia and the parallel shift axis equation; $e_{y'}$, h_{b} and y_{flange} are the distance from the center to the edge of the T-stiffened plate, the distance between two T-stiffened plates and the distance from the center of the T-stiffened plate to the neutral axis, respectively.

$$A_{\text{flange}} = (B-b)c + bh \tag{18}$$

$$I_{\text{flange}} = \frac{1}{3}\left[(B-b)c^3 + bh^3\right] - e_{y'}^2 A_{\text{flange}} \tag{19}$$

$$I_{\text{b,flange}} = I_{\text{flange}} + y_{\text{flange}}^2 \cdot A_{\text{flange}} \tag{20}$$

$$P_{\text{y1-flange}} = \frac{2 f_y I_{\text{b,flange}}}{y_{\text{flange}} L_p} \tag{21}$$

When the T-stiffened plate is buckling, the regularized slenderness ratio λ_{n} is calculated by bringing the slenderness ratio λ into Eq. (22), the section type of the T-stiffened plate is b class, and the stability coefficient ϕ of the T-stiffened plate is calculated by combining the determination coefficients α_1, $\alpha_2$and α_3 of the specification GB50017-2017[30], which are used in Eq. (25) to obtain $P_{\text{y2-flange}}$. Finally, the smaller values of Eqs (21) and (25) are taken as the yield capacity of the T-stiffened plate $P_{\text{y-flange}}$, as shown in Eq. (26).

$$\lambda_n = \frac{\lambda}{\pi}\sqrt{\frac{f_y}{E}} \tag{22}$$

$$\lambda_n \le 0.215 \qquad \varphi = 1 - \alpha_1 \lambda_n^2 \tag{23}$$

$$\lambda_n > 0.215 \qquad \varphi = \frac{1}{2\lambda_n^2}\left[(\alpha_2 + \alpha_3\lambda_n + \lambda_n^2) - \sqrt{(\alpha_2 + \alpha_3\lambda_n + \lambda_n^2)^2 - 4\lambda_n^2}\right] \tag{24}$$

$$P_{y2-\text{flange}} = 2\varphi A_{\text{flange}} f_y y_{\text{flange}} / L_p \tag{25}$$

$$P_{y-\text{flange}} = min\left(P_{\text{y1-flange}}, P_{\text{y2-flange}}\right) \tag{26}$$

The slit plate requires the calculation of the edge rib contribution to the damper's yielding capacity, a process akin to that for the T-stiffened plate, with identical calculations for yielding and buckling. When yielding occurs at the edges of the slit plate, it is calculated according to equations (27) to (29), where $y_{\text{slit-1}}$ is the distance from the center of the cross-section shape to the neutral axis. Slit plate edge buckling occurs, calculate the rib length to slenderness ratio λ brought into the Eqs. (22) ~ (24) to obtain the stability coefficient ϕ, brought into the Eqs. (30) ~ (31). To take the smaller value of the two as the slit plate $P_{\text{y-slit}}$, calculate the corrugated plate $P_{\text{y-corrugated}}$ similarly as shown in Eq. (32). The $P_{\text{y-slit}}$ and $P_{\text{y-corrugated}}$ are added to $P_{\text{y-flange}}$ to obtain the yield capacity P_{yc} of the slit damper and corrugated damper, respectively, as shown in Eq. (33). Combined with the failure mode of the metal damper, it can

be seen that the middle part of the T-stiffened plate and both sides of the slit plate or corrugated plate undergo obvious out-of-plane bending deformation, and due to the existence of the hinges, the center of the slit plate or corrugated plate does not have obvious plastic deformation, but it still reaches the yield state. Therefore, it is still necessary to consider the contribution of the slit plate or corrugated plate at the center of rotation to the bearing capacity when calculating the peak bearing capacity of the metal damper. The full-section yielding is used to calculate the peak bearing capacity P_{mc} of the metal damper, as shown in Eq. (34), where f_y is the steel yield strength; WP is the modulus of the plastic section, and L_p is the lever arm. The results of P_{yc} and P_{mc} calculations are summarized in **Fig. 22**.

$$A_{\text{slit-1}} = t \cdot b_{\text{slit-1}} \tag{27}$$

$$I_{\text{slit-1}} = \frac{t b_{\text{slit-1}}^3}{12} + A_{\text{slit-1}} y_{\text{slit-1}}^2 \tag{28}$$

$$P_{\text{y1-slit-1}} = \frac{4 f_y I_{\text{slit-1}}}{y_{\text{slit-1}} L_p} \tag{29}$$

$$P_{y2-\text{slit-1}} = 2\varphi A_{\text{slit-1}} f_y y_{\text{slit-1}} / L_p \tag{30}$$

$$P_{y-\text{slit}} = min\left(P_{\text{y1-slit-1}}, P_{\text{y2-slit-1}}\right) \tag{31}$$

$$P_{y-\text{corrugated}} = A_{y-\text{corrugated-1}} \cdot f_y \cdot y_{\text{corrugated-1}} / L_p \tag{32}$$

$$P_{\text{yc}} = \begin{cases} P_{y-\text{flange}} + P_{y-\text{slit}} \\ P_{y-\text{flange}} + P_{y-\text{corrugated}} \end{cases} \tag{33}$$

$$p_{\text{mc}} = f_{\text{y}} W_{\text{p}} / L_{\text{p}} \tag{34}$$

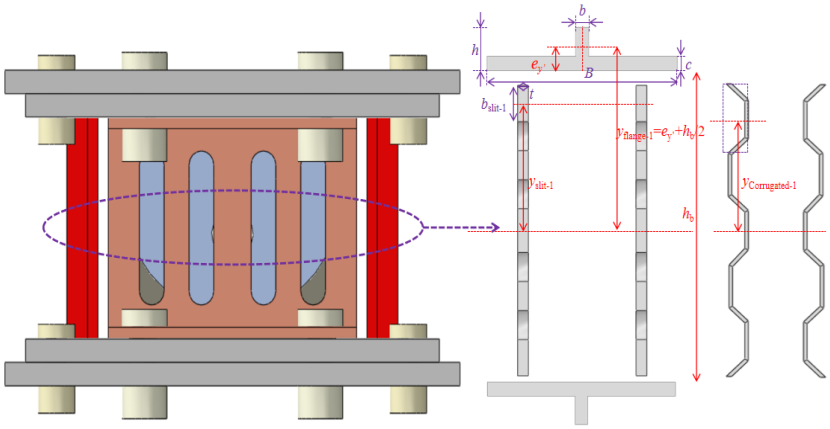

Fig.21 Section size of damper

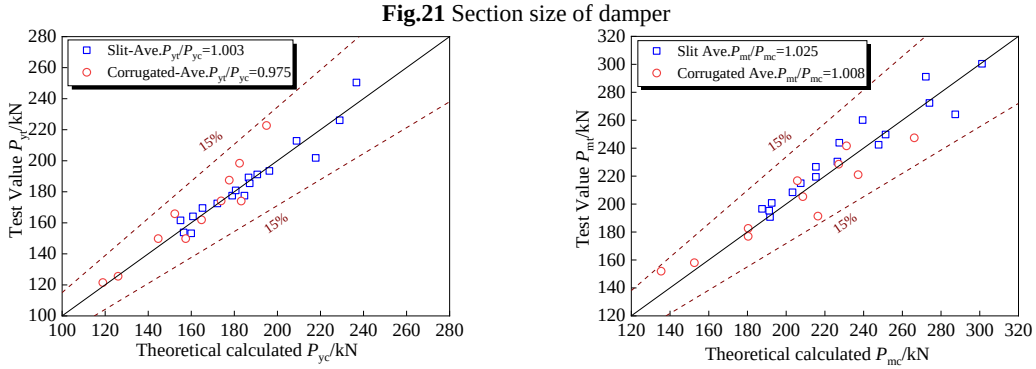

(a)Yield bearing capacity (b) Peak bearing capacity

Fig.22 Calculation result of bearing capacity

4.3Dimensionless skeleton curve model

The skeleton curves from the experimental and numerical simulations of the metal damper are normalized to obtain the pre-peak OA and AB segments and the post-peak BC segment by linear fitting, such that the curves pass through points O (0,0) and B (1,1). A dimensionless skeleton curve is formed, as shown in **Fig. 23**, and the mathematical expressions of each segment are Eqs. (35)~(36). Combined with the calculation results of initial stiffness K, yield-bearing capacity P_y, and peak bearing capacity P_m in sections 4.1~4.2, as shown in **Fig. 24**, the theoretical calculation skeleton curve of the metal damper is obtained. To validate the proposed skeletal curves model, a comparison is conducted among experimental, numerical simulation, and theoretically calculated skeletal curves, as depicted in **Fig. 25**. The proposed methodology adequately represents the mechanical behavior of both slit and corrugated dampers, providing a theoretical reference for practical engineering applications of metal dampers.

$$\begin{cases} \text{OA:}\ P/P_m = 4.1484\Delta/\Delta_m \\ \text{AB:}\ P/P_m = 0.2576\Delta/\Delta_m + 0.7418 \\ \text{BC:}\ P/P_m = -0.2251\Delta/\Delta_m + 1.2312 \end{cases} \tag{35}$$

$$\begin{cases} \text{OA:}\ P/P_m = 2.6267\Delta/\Delta_m \\ \text{AB:}\ P/P_m = 0.2947\Delta/\Delta_m + 0.7052 \\ \text{BC:}\ P/P_m = -0.1424\Delta/\Delta_m + 1.134 \end{cases} \tag{36}$$

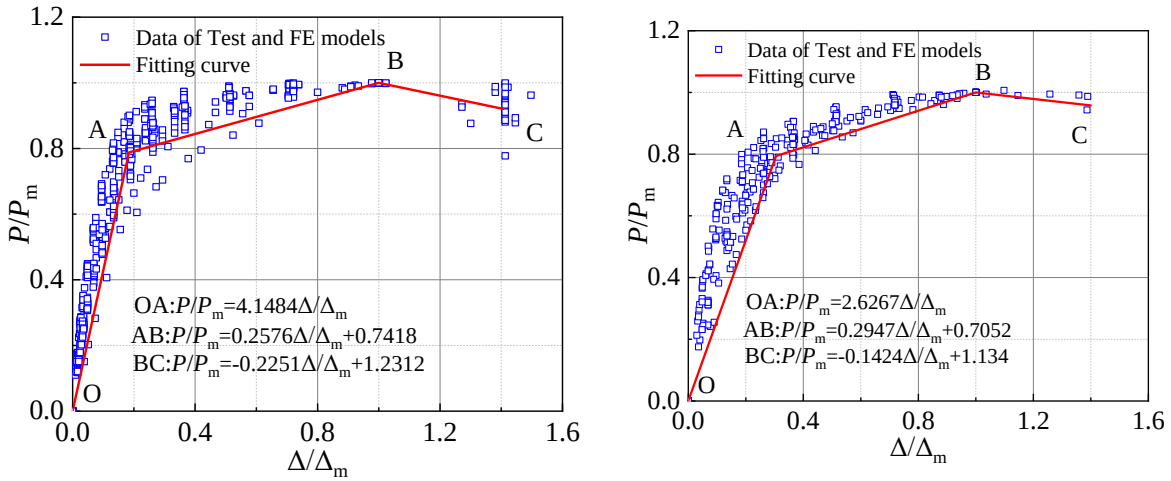

(a)Slid damper (b)Corrugated damper

Fig.23 Dimensionless skeleton curve

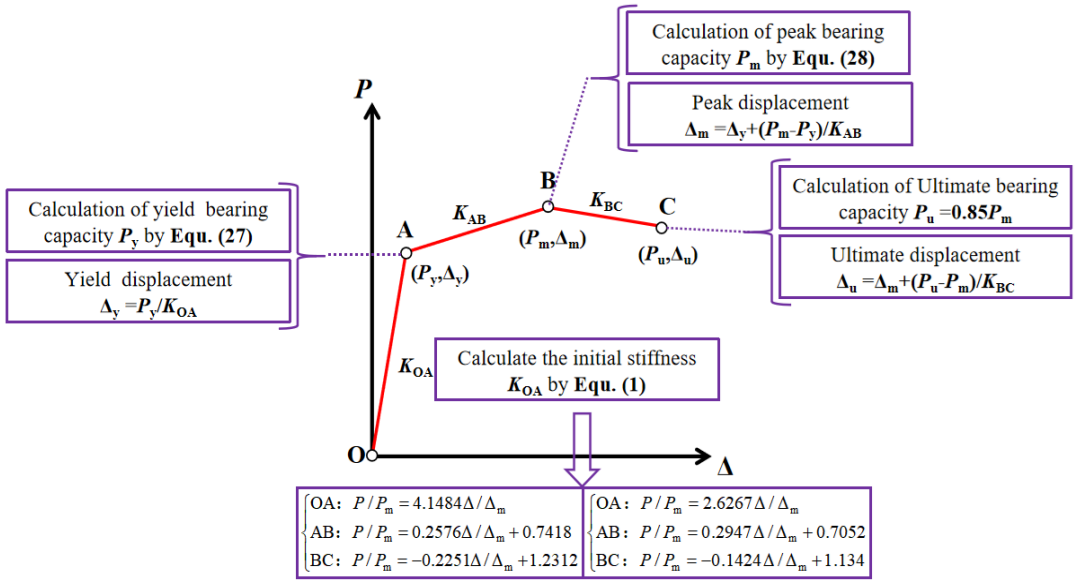

Fig.24 Calculation process

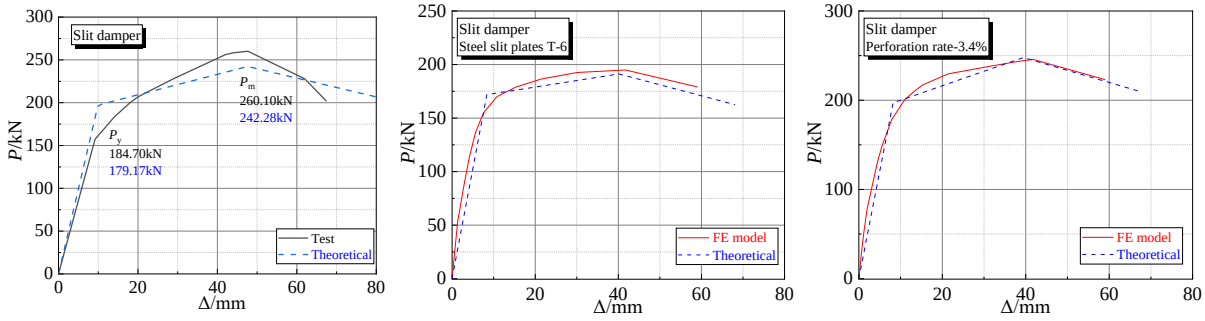

(a)Slid damper

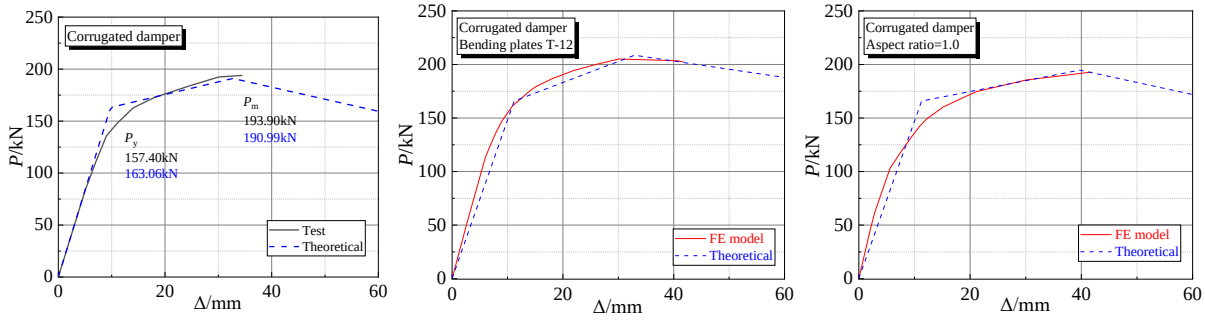

(b)Corrugated damper

Fig.25 Validation of skeleton curve model

5. Conclusions

Based on the post-earthquake replaceability design concept, two types of metallic dampers for beam-column joints were proposed. Through experimental and numerical simulations, this study investigated the yield mechanism, damage distribution, and peak bearing capacity of these slit /corrugated damper, and established a skeleton curve model for metallic dampers. The following conclusions can be drawn from current research findings:

[1] The slit damper exhibits a sequential yielding characteristic, wherein the T-stiffened plate first enters into plastic deformation, followed by energy dissipation occurring at both ends of the slitted plate. This process manifests as a gradual yielding behavior. By contrast, the yielding sequence of the corrugated damper is less distinct due to the thinner gauge of the corrugated plate. In addition, the positive and negative peak bearing capacity (P_m) of the slit damper is 11.82% and 34.14% higher than that of the corrugated damper, respectively.

[2] Integrating steel hinges into the energy dissipation device allows it to bear 55% to 87% of the shear force. This integration effectively delays plastic damage to the slit and corrugated plates, thereby providing a certain safety margin for component replacement and post-earthquake repair.

[3] A parametric study was conducted to investigate the influence of key parameters, including the aspect ratio and thickness of the T-stiffened plate, the thickness of the slit/corrugated plate, and the perforation ratio of the slit plate. Among these parameters, the aspect ratio and thickness of the T-stiffened plate significantly affect the peak bearing capacity of the metallic damper. When the aspect ratio of the T-stiffened plate exceeds 1.27, it leads to earlier plastic yielding of the slit and corrugated plates, reducing the overall peak bearing capacity. Furthermore, the thickness of the T-stiffened plate should not be less than that of the slit or corrugated plate and should not exceed 16 mm within the scope of this study.

[4] Increasing the thickness of both the slit plates and corrugated plates significantly enhances peak bearing capacity and initial stiffness. Notably, when the thickness of the corrugated plates is increased from 3mm to 9mm, their initial stiffness improves by 15.34% and 10.91%, respectively. The increase in the thickness of the corrugated plate can effectively alleviate corner buckling, so it is recommended that the thickness of the corrugated plate be higher than 3mm. Furthermore, to ensure

that the slit damper has an optimal bearing capacity and deformation capacity, it is reasonable to control the perforation ratio so that it does not exceed 14.9%.

[5] The derivation of the initial stiffness calculation formulas for two categories of metal dampers considered the contributions of the T-stiffened plate, high-strength bolts, slit plate, and corrugated plate to the initial stiffness. The accuracy of the initial stiffness model was verified by comparing experiments, simulations, and theoretical calculations with the average values of the initial stiffness, which were 1.002 and 1.068, respectively.

[6] The skeleton curve models for slit and corrugated dampers are established. The key points of the skeleton curves are determined by considering bearing capacity. The results demonstrate that the proposed skeleton curves can effectively reflect the mechanical properties of slit and corrugated dampers. These skeleton curves provide a theoretical basis for the engineering application of such metal dampers.

Acknowledgement

The authors thank the National Natural Science Foundation of China (No. 52378197) and the Doctoral Dissertation Innovation Fund of Xi ́an University of Technology (No. 252072301).

Funding Statement

The authors received no specific funding for this study.

CRediT authorship contribution statement

Hongchao Guo:Investigation, Methodology, Funding acquisition, Writing-review & editing, Supervision. **Yuwei Li**:Data analysis & processing, Writing-original draft, Writing-review & editing, calculating method,Visualization. **Dongdong Zheng**: Calculating method, & editing. **Wenqi Wang**: Formal analysis, & Visualization. **Renzhang Song**: Calculating method, & editing. **Yunhe Liu:** Formal analysis, & editing.

Conflicts of Interest

The authors declare that they have no conflicts of interest to report regarding the present study.

Data Availability Statement

Some or all data, models, or codes that support the findings of this study are available from the corresponding author upon reasonable request.

References

[1] Yang QM, Ban HY. Balanced design philosophy of superior high-performance steel cover-plated beam-to-column joints. Thin-Walled Structures 2023, 184: 110470. https://doi.org/10.1016/j.tws.2022.110470.

[2] Pachoumis DT, Galoussis EG., Kalfas CN. Reduced beam section moment connections subjected to cyclic loading: Experimental analysis and FEM simulation. Engineering Structures 2009, 31:216–223. https://doi.org/10.1016/j.engstruct.2013.11.010.

[3] Liang G, Lu ZH, Guo HC, Liu YH, Yang DX, Li S, Pan XZ. Experimental and numerical investigation on seismic performance of extended stiffened end-plate joints with reduced beam section using high strength steel .Thin-Walled Structures 2021, 169:108434. https://doi.org/10.1016/j.tws.2021.108434.

[4] Guo HC, Zhou XZ, Li W, Liu YH, Yang DX. Experimental and numerical study on seismic performance of Q690 high-strength steel plate reinforced joints. Thin-Walled Structures 2021, 161: 107510. https://doi. org/10.1016/j.tws.2021.107510.

[5] Guo HC, Xie Y, Tian JB, Kou JL. Seismic behavior of assembled beam-column joints with C-shaped cantilever section. Journal of Constructional Steel Research 2021, 183: 106766. https://doi.org/10.1016/j. jcsr.2021. 10 6766.

[6] Wu ZL, Lu XL, Cai ZW, Li LZ, Yu KQ, Lu ZD. Post-earthquake fire resistance of self-centering concrete beam-column joint: An experimental investigation. Engineering Structures 2024, 305: 117689. https://doi. o rg/10.1016/j.engstruct.2024.117689.

[7] Lu X, Sun WH, Xu LH. Experimental investigation on seismic behavior of damaged self-centering friction beam-column joints after repair. Engineering Structures 2024, 310: 118135. https://doi.org/10.1016/j. engstr uct.2024.118135.
[8] Ru YC, He LS. Seismic behavior of a self-centering beam-to-column joint using low-yield arc steel plates for dissipating energy. Journal of Building Engineering 2024, 95: 110117. https://doi.org/10.1016/j.j obe.2024. 110117.
[9] Zhang L, Zhang ZY, Zhou Y, Chen YF, Tong GS, Jiang X, Li WB. Experimental study on edge cell partially-replaced joint for I-beam to multi-celled CFST walls under cyclic loading. Journal of Building Engineering 2024, 91: 109443. https://doi.org/10.1016/j.jobe.2024.109443.
[10] Ye YX, Wang ZB, Yang ZH, Hou ZY, Qiao PS. Seismic performance test research on a new type of replaceable energy-consuming joint column. Soil Dynamics and Earthquake Engineering 2023, 166: 107786. https://doi.org/10.1016/j.soildyn.2023.107786.
[11] Wang ZB, Kang Q, Ye YX. Experimental study on the seismic performance of a fully assembled column base node with a replaceable energy-consuming joint. Journal of Building Engineering 2023, 68: 106165. https://d oi.org/10.1016/j.jobe.2023.106165.
[12] Hao H, Bi KM, Chen WS, Pham TM, Li J. Towards next generation design of sustainable, durable, multi-hazard resistant, resilient, and smart civil engineering structures. Engineering Structures 2023, 277: 115477. https://doi.org/10.1016/j.engstruct.2022.115477.
[13] Sun DD, Yang Y, Ma YK, Xue YC, Yu YL, Feng SQ. Seismic behavior of self-centering column base with replaceable stiffener angle steels. Thin-Walled Structures 2022, 181: 110113. https://doi.org/10.1016/j.tw s.2 022.110113.
[14] Huang JH, Zhu SY, Wang B. Self-centering steel beam-to-column connections with novel super elastic SMA angles. Journal of Constructional Steel Research 2024, 214: 108458. https://doi.org/10.1016/j.jc sr.2024.108 458.
[15] Men JJ, Li T, Zhou Q, Zhang HH, Huang CH. Structural fuse performance and earthquake-resilient performance of beam-column joints with replaceable T-stub. Journal of Constructional Steel Research 2023, 206: 107943. https://doi.org/10.1016/j.jcsr.2023.107943.
[16] Qi YH, Teng J, Shan QF, Ding JP, Li ZH, Huang CG, Xing HB, Yi WQ. Seismic performance of a novel prefabricated beam-to-column steel joint considering buckling behaviour of dampers. Engineering Structures 2021, 229: 111591. https://doi.org/10.1016/j.engstruct.2020.111591.
[17] Felice CP, Di CA, Lamarucciola N, Domenico N. Experimental estimation of energy dissipated by multistorey post-tensioned timber framed buildings with anti-seismic dissipative devices. Sustainable Structures 2021: 2789-3111. 10.54113/j.sust.2021.000007.
[18] Wang CQ, Li HH, Xu L, Xu KX, Zhao LC , Chen Q. Seismic performance of PS-CFST bridge piers with novel external replaceable energy dissipating devices. Journal of Constructional Steel Research 2025, 224: Part A, 109156. https://doi.org/10.1016/j.jcsr.2024.109156.
[19] Wang CQ, Qu Z, Shen YG, Ping BY, Xie J. Cyclic Testing on Seismic Behavior of Segmental Assembled CFST Bridge Pier with External Replaceable Energy Dissipator. Metals 2022, 12(7): 1156. https://doi.org/10 .3390/met12071156.
[20] Hu GX, Zhang ZY, Cao B, Pan ZC, Zeng L. Seismic behavior of precast concrete beam-column joints with bending moment-shear separation controllable plastic hinge. Engineering Structures 2024, 304: 117585. htt ps://doi.org/10.1016/j.engstruct.2024.117585.
[21] Li ZH, Qi YH, Teng J. Experimental investigation of prefabricated beam-to-column steel joints for precast concrete structures under cyclic loading. Engineering Structures 2020, 209: 110217. https://doi.org/10. 1016 /j.engstruct.2020.110217.
[22] Xie LQ, Wu J, Zhang JY, Liu CY. Experimental study of mechanical properties of beam-column joint of a replaceable energy-dissipation connector-precast concrete frame. Journal of Building Engineering 2021, 43: 102588. https://doi.org/10.1016/j.jobe.2021.102588.
[23] Du YF, Li FY, Li H, Hong N, Chi PH. Seismic behavior and resilience assessment of prefabricated beam-column joint with replaceable graded-yielding energy-dissipating connectors. Engineering Structures 2024, 319: 118814. https://doi.org/10.1016/j.engstruct.2024.118814.
[24] Yang CT, Li AQ. Experimental investigation on seismic performance of double-stage-behavior dry-connected beam-to-column joint. Engineering Mechanics 2024, 41: 1000-4750. 10.6052/j.issn.1000-4750.2022.02.0187 (in Chinese).
[25] Hu GX. Seismic Performance of Precast RC Beam-column joints and Prefabricated Frame Structures with Replaceable Energy Dissipation Connection. Xi'an University of Architecture and Technology. China, Xi’an, 2022.
[26] Wang JT, Sun Q, Li YW, Liu XH. Hysteretic performance of circular high-strength concrete-filled double skin steel tubular columns: Experiment. Marine Structures 2024, 93: 103519. https://doi.org/10.1016/j.mars truc.2023.103519.

[27] FEMA, Interim Testing Protocols for Determining the Seismic Performance Characteristics of Structural and Nonstructural Components (FEMA-461), Federal Emergency Management Agency, Washington, DC, 2007.
[28] Chaboche J L. Time independent constitutive theories for cyclic plasticity. International Journal of Plasticity 1986, 2(2):149-188.https://doi.org/10.1016/0749-6419(86)90010-0.
[29] Shi YJ, Wang M,Wang YQ. Experimental study of structural steel constitutive relationship under cyclic loading. Journal of building materials 2012, 15(03):293-300. 10.3969/j.issn.1007-9629.2012.03.001.(in Chinese).
[30] GB 50017-2017. Standard for Design of Steel Structures. Beijing, China: China Architecture & Building Press; 2017 (in Chinese).
[31] EN 1993-1-8. Eurocode 3: Design of Steel Structures Part 1-8: Design of Joints , European Committee for Standardization, Brussels, 2005.